Characterization of graphene through anisotropy of constant-energy maps in angle-resolved photoemission

M. Mucha-Kruczyński,[1] O. Tsyplyatyev,[1,*] A. Grishin,[1] E. McCann,[1] Vladimir I. Fal'ko,[1,2] Aaron Bostwick,[3] and Eli Rotenberg[3]

[1]*Department of Physics, Lancaster University, Lancaster LA1 4YB, United Kingdom*

[2]*LPS-CNRS, University of Orsay, F-91405 Orsay cedex, France*

[3]*Advanced Light Source, MS 6-2100, Lawrence Berkeley National Laboratory, Berkeley, California 94720, USA*

(Received 30 November 2007; published 1 May 2008)

We theoretically show how constant-energy maps of the angle-resolved photoemission intensity can be used to test wave function symmetry in graphene. For monolayer graphene, we demonstrate that the observed anisotropy of angle-resolved photoelectron spectroscopy spectra is a manifestation of what has been recently branded as an electronic chirality. For bilayer graphene, we show that the anisotropy of the constant-energy maps may be used to extract information about the magnitude and sign of interlayer coupling parameters and about symmetry breaking inflicted on a bilayer by the underlying substrate.

DOI: 10.1103/PhysRevB.77.195403 PACS number(s): 79.60.−i, 73.22.−f, 81.05.Uw, 73.43.Cd

I. INTRODUCTION

Four years ago, the fabrication of ultrathin graphitic devices,[1] including monolayers and bilayers, followed by observations[2–4] of the classical and quantum Hall effects, led to an explosion of interest in monolayer graphene. This material is a two-dimensional layer of carbon atoms arranged on a honeycomb lattice [Fig. 1(a)]. In a nominally undoped sample, states at the Fermi level lie at the corner of the first Brillouin zone, which is known as K points or valleys [Fig. 1(b)], where the energy spectrum is degenerate. By doping or by applying a back gate,[1–4] it is possible to adjust the density of electrons in the graphene sample so that states at the Fermi level lie in the vicinity of the valley where the electronic spectrum is approximately conical [Fig. 1(c)]. It has also been possible to fabricate graphene bilayers, which, by way of contrast with monolayers, have an approximately parabolic dispersion at low energy[4,5] and specific properties detected in transport.[4,6–8]

The linear dispersion of electrons in graphene[9–11] has drawn a formal analogy with the dynamics of relativistic massless particles, which has been broadly discussed in the literature.[12–14] The combination of a sublattice composition of electronic Bloch states (treated as an "isospin") in a single atomic sheet of graphite with a linear dispersion in the vicinity of the corners of the Brillouin zone makes them chiral, similar to Dirac fermions. Experimentally, the chiral nature of charge carriers has been deduced from a peculiar sequencing of plateaus in the quantum Hall effect,[1–4] while the linear dispersion relation has been directly observed by angle-resolved photoelectron spectroscopy (ARPES).[5,15–21] ARPES has already been used to provide information about the form of the dispersion curves, renormalization of spectra by electron-electron and electron-phonon interactions, and information about quasiparticle lifetimes in the material.[15,22,25]

On the basis of the theory presented in this paper, we point out that constant-energy angular maps of photoemission reflect the chirality discussed in relation to charge carriers in graphene. For monolayers, we show that the recently published ARPES data provide evidence of the chirality of carriers in this material. We theoretically demonstrate that the anisotropy of the constant-energy maps may be used to extract information about the magnitude and sign of interlayer coupling parameters in bilayer graphene and about the types of symmetry-breaking effects produced by the underlying substrate or doping. In particular, we demonstrate that one can distinguish between two effects that may generate a gap in the bilayer spectrum: interlayer asymmetry[5,7,8,26–34] and symmetry breaking at the bottom layer, which rests on a SiC substrate.[18,19,35]

Whereas the chirality of a relativistic particle is defined by its spin, chirality in graphene refers to the sublattice composition of plane-wave states of Bloch electrons. The honeycomb lattice of monolayer graphene [Fig. 1(a)] has two sites in the unit cell, which are labeled as A and B. Usually, its Brillouin zone is also chosen in the most symmetric hexagonal form [dashed lines in Fig. 1(b)], however, for simplicity of the following ARPES analysis we choose the Brillouin zone to be in the form of a rhombus (solid lines), which uniquely defines momentum values for the K-points, $\mathbf{K}_{\pm} = \pm(4\pi/3a, 0)$, also referred to as centers of valleys [Fig. 1(b)]. Near the center of the valley, e.g., K_+ in monolayer graphene, electrons are described by a Dirac-type Hamiltonian,

$$\hat{\mathcal{H}}_1 \approx \hbar v \boldsymbol{\sigma} \cdot \mathbf{q}, \tag{1}$$

which determines the linear dispersion $\epsilon = \hbar v q$ of electrons in the conduction band and $\epsilon = -\hbar v q$ in the valence band.[9] The eigenstates Ψ, within a single valley, have different amplitudes on the adjacent A and B sites, and by following the example of relativistic physics, they may be written as a two-component "spinor" $\Psi = (\psi_A, \psi_B)$. The chirality of a relativistic particle is right handed if its spin points in the same direction as its momentum, while its chirality is left handed if its spin points in the opposite direction. By analogy, the relative phase ϕ between the wave functions on sublattice atoms indicates the isospin vector $\boldsymbol{\sigma} = (\cos\phi, \sin\phi, 0)$ of the chiral state $\Psi = (e^{-i\phi/2}, e^{i\phi/2})$ of quasiparticles in graphene.

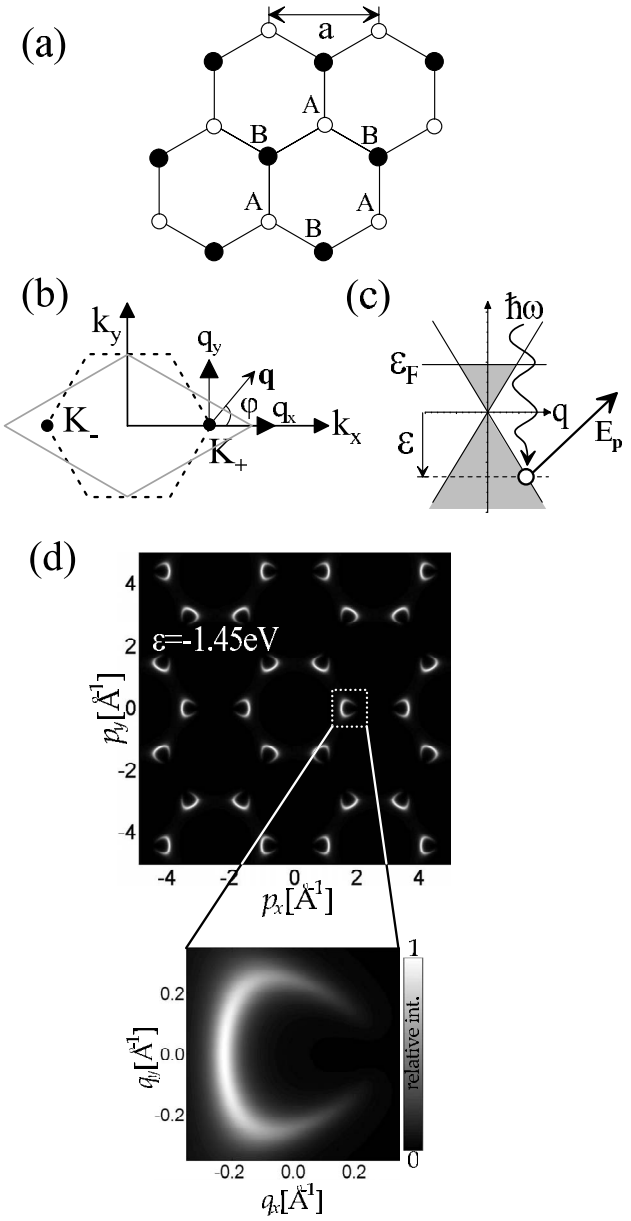

FIG. 1. (a) Schematic of the monolayer lattice containing two sites in the unit cell: A (white circles) and B (black circles). (b) Schematic of the hexagonal and rhombic Brillouin zone indicating two inequivalent valleys $K_\pm$ showing the wave vector $\mathbf{q}=(q\cos\varphi, q\sin\varphi)$ measured from the center of valley K_+. (c) Schematic of the low energy bands $\epsilon\approx\pm\hbar vq$ near the K_+ point obtained by taking into account intralayer hopping with velocity v. The shading indicates the region of occupied states up to the Fermi energy ϵ_F and the dashed line indicates a typical energy of states contributing to photoemission, whereby incoming photons of energy $\hbar\omega$ produce photoelectrons of kinetic energy $E_\mathbf{p}$. (d) The intensity of photoemission from states at a constant energy of 1.4 eV below the charge-neutrality point (Ref. 38) in monolayer graphene, which is plotted as a function of photoelectron wave vector $\mathbf{p}_\parallel=(p_x,p_y)$ parallel to the surface of graphene for $\mathbf{p}_\parallel$ covering several Brillouin zones (top) and plotted as a function of photoelectron wave vector $\mathbf{q}=(q_x,q_y)$ in the vicinity of valley K_+ (bottom) [note that the origin and scale of $\mathbf{p}_\parallel$ and $\mathbf{q}$ are different]. Here, we use the parameter values $\gamma_0=3.0$ eV, $s_0=0.129$, $\Delta=0$, and energy width $\Gamma=0.24$ eV.

TABLE I. Manifestation of electronic chirality in the anisotropy of ARPES constant-energy maps in monolayer graphene in the valley K_+, where ϕ is the sublattice phase difference and angle φ specifies the direction of the electronic wave vector measured from the center of the valley [see Fig. 1(b)].

Energy ϵ_q	Chirality $\sigma\cdot\mathbf{n}_1$	Sublattice phase difference	ARPES anisotropy
$+vq$	$+1$	$\phi=\varphi$	$I\sim\cos^2(\varphi/2)$
$-vq$	-1	$\phi=\varphi+\pi$	$I\sim\sin^2(\varphi/2)$

ARPES[36,37] is exactly the tool to visualize this state through the angular dependence of the emitted photoelectron flux.

The proposed analysis is based on the standard theory of angle-resolved photoemission.[36,37] In an ARPES experiment, incident photons with energy $\hbar\omega$ produce photoelectrons whose intensity I is measured in a known direction as a function of kinetic energy $E_\mathbf{p}\approx\hbar^2(|\mathbf{p}_\parallel|^2+p_z^2)/2m$:[36,37] $\hbar\omega=E_\mathbf{p}+A-\epsilon_q$, where A is the work function and ϵ_q is the energy of Bloch electrons in graphene. Conservation of momentum ensures that the component of the momentum parallel to the graphene surface $\hbar\mathbf{p}_\parallel=\hbar(p_x,p_y)$ is equal to the quasimomentum $\hbar\mathbf{K}_\pm+\hbar\mathbf{q}$ of Bloch electrons near valley $K_\pm$,

$$\mathbf{p}_\parallel=\mathbf{K}_\pm+\mathbf{q}+\mathbf{G}, \tag{2}$$

where $\mathbf{q}$ is the wave vector measured from the center of the valley $K_\pm$ and a reciprocal lattice vector $\mathbf{G}=m_1\mathbf{b}_1+m_2\mathbf{b}_2$ is written in terms of primitive reciprocal lattice vectors $\mathbf{b}_1=(2\pi/a,2\pi/\sqrt{3}a)$ and $\mathbf{b}_2=(2\pi/a,-2\pi/\sqrt{3}a)$ and integers m_1 and m_2.

As graphene has two inequivalent atomic sites, the angular dependence of the intensity may be accounted for by considering two-source interference (*à la* Young's double slits). Outside the sample at a position $\mathbf{R}_0$ relative to the midpoint of the two sources, electronic waves $e^{[i\mathbf{p}\cdot(\mathbf{R}_0+\mathbf{u}/2)-i\phi/2]}$ and $e^{[i\mathbf{p}\cdot(\mathbf{R}_0-\mathbf{u}/2)+i\phi/2]}$ from the adjacent A and B sites combine. This yields the intensity I of the two-source interference pattern,

$$I\sim\cos^2\left[\frac{\mathbf{p}_\parallel\cdot\mathbf{u}}{2}-\frac{\phi}{2}\right], \tag{3}$$

where $\mathbf{u}=(0,a/\sqrt{3})$ is the separation of the adjacent sites, and near each corner of the Brillouin zone, $\mathbf{p}_\parallel\cdot\mathbf{u}\approx2\pi(m_1-m_2)/3$. The first term in the argument of Eq. (3) is a phase difference due to the different path lengths of electron waves that are emitted from two sublattices, while the second term $-\phi/2$ arises from the relative phase of the electronic Bloch states on A and B sublattices that are determined by the quasiparticle chirality.

Electrons in the conduction and valence bands at the valley K_+, which are determined by the Dirac Hamiltonian [Eq. (1)], differ by the projection of their isospin onto the direction of their wave vector $\mathbf{q}=(q\cos\varphi,q\sin\varphi)$, as described by the chiral operator $\sigma\cdot\mathbf{n}_1$, where $\mathbf{n}_1(\mathbf{q})=(\cos\varphi,\sin\varphi)$: $\sigma\cdot\mathbf{n}_1=1$ in the conduction band and $\sigma\cdot\mathbf{n}_1=-1$ in the valence band, as listed in Table I. Note that the first term in the

argument of Eq. (3), which arises from the path difference between electron waves emitted from two sublattices, accounts for the relative rotation in the interference pattern around the six corners of the hexagonal Brillouin zone. Figure 1(d) shows a typical calculated dependence of the intensity of the photoemission from states (here, at energy 1.45 eV below the charge-neutrality point[38]) plotted as a function of wave vector $\mathbf{p}_\parallel$, which is in agreement with the qualitative prediction of the two-source interference picture [Eqs. (1) and (3)] summarized in Table I. The numerical results of calculations [Fig. 1(d)] appear to be consistent with the experimentally measured constant-energy maps.[15]

So far, we have discussed the angular dependence of the interference patterns, neglecting the effect of the anisotropy of the band structure, which is known as trigonal warping. It leads to a triangular deformation of isoenergetic lines in the band structure of graphene and the $\epsilon_q(-\mathbf{q}) \neq \epsilon_q(\mathbf{q})$ asymmetry of the electron dispersion around each valley, which becomes more pronounced for states further from the charge-neutrality point. Another perturbation of chiral particles in graphene may be an asymmetry $\Delta = \epsilon_A - \epsilon_B$ of on-site lattice energies ϵ_A and ϵ_B due to the presence of a substrate, which leads to a gap Δ in the spectrum at low energies. The presence of such asymmetry in graphene that is epitaxially grown on a SiC substrate and the possibility of observing its effect within spectroscopic accuracy was recently discussed following experimental ARPES measurements of a low-energy band structure.[18,19] In Sec. II below, we show that opening an *AB* asymmetry gap in the monolayer spectrum is accompanied by the loss of the chirality-related anisotropy of ARPES angular maps at low energies, which can be used as an additional test for the symmetry-breaking effect induced by a SiC substrate.

In Sec. III, we offer a detailed analysis of the angle-dependent maps of ARPES of bilayer graphene for such incident photon energies that $p_z d \ll 1$ for the photoemitted electrons (d is the interlayer spacing in the bilayer). First, we analyze angular photoemission maps of an ideal "pristine" bilayer by taking into account intricate details of its band structure and by using a tight-binding model that employs the Slonczewski–Weiss–McClure parametrization of relevant couplings.[10,11] In Secs. III A and III B, we show that angular maps can be used to determine not only the magnitude but also signs of the interlayer coupling constants that are used in the tight-binding model. If experimentally measured, the latter information may also prove to be useful for general studies of bulk graphite. In Sec. III C, we analyze the influence of interlayer and intralayer symmetry breakings in bilayers, and we show that the effect of the interlayer charge transfer upon doping can be, in principle, distinguished from crystalline asymmetry that is induced by a SiC substrate. In Sec. III D we analyze the dependence of the constant-energy maps on the incident photon energy. This is due to the modification of the interference pattern by the additional vertical distance traveled by the electron originating from the bottom layer.

II. PHOTOEMISSION FROM MONOLAYER GRAPHENE

To produce a quantitative prediction of the photoemission intensity, we use the Fermi golden rule to calculate the probability of a photostimulated transition from an initial band state with two-dimensional quasimomentum $\hbar\mathbf{k} = \hbar\mathbf{K}_\pm + \hbar\mathbf{q}$ and energy $\epsilon_\mathbf{q}$ in graphene to a continuum state with momentum $\hbar\mathbf{p}$ and energy $E_\mathbf{p}$ in vacuum.[36] The initial state wave function in graphene is written as a linear combination of Bloch wave functions on A and B sublattices with coefficients ψ_A and ψ_B, respectively,

$$\Psi_\mathbf{k}(\mathbf{r}) = \sum_{j=A,B} \psi_j(\mathbf{k}) \left[\frac{1}{\sqrt{N}} \sum_{\mathbf{R}_j} e^{i\mathbf{k}\cdot\mathbf{R}_j} \Phi(\mathbf{r} - \mathbf{R}_j) \right],$$

where $\mathbf{R}_A$ and $\mathbf{R}_B$ are the positions of A- and B-type atoms and $\Phi(\mathbf{r})$ is a p_z atomic orbital. Then, the intensity I of photoemission from states in a given band may be written as

$$I \sim |\Phi_\mathbf{p}|^2 \left| \sum_j \psi_j e^{-i\mathbf{G}\cdot\tau_j} \right|^2 \delta(E_\mathbf{p} + A - \epsilon_q - \omega), \tag{4}$$

where $\Phi_\mathbf{p} = \int e^{-i\mathbf{p}\cdot\mathbf{r}} \Phi(\mathbf{r}) d^3r$ is the Fourier image of an atomic orbital $\Phi(\mathbf{r})$, and the wave vector component parallel to the surface is conserved, i.e., $\mathbf{q} = \mathbf{p}_\parallel - \mathbf{K}_\pm - \mathbf{G}$ [Eq. (2)]. The summation with respect to index $j = \{A, B\}$ takes into account the coefficients ψ_A and ψ_B, which are located at atomic positions defined by basis vectors $\tau_A = -\mathbf{u}/2$ and $\tau_B = \mathbf{u}/2$ within a given unit cell. The Dirac delta function, which contains the work function of graphene A, expresses energy conservation. In this paper, note that we do not model dynamical effects that lead to energy broadening[15,22–25] but introduce a Lorentzian $\delta(\cdots) \approx \Gamma/(\pi[(\cdots)^2 + \Gamma^2])$ in the figures with the parameter Γ representing finite energy broadening.

A standard form[39,40] of a tight-binding monolayer Hamiltonian $\hat{H}_1$ and overlap-integral matrix $\hat{S}_1$ (that takes into account the nonorthogonality of orbitals on adjacent atomic sites), $\hat{H}_1\Psi = \epsilon_\mathbf{q}\hat{S}_1\Psi$, is

$$\hat{H}_1 = \begin{pmatrix} \Delta/2 & -\gamma_0 f(\mathbf{k}) \\ -\gamma_0 f^*(\mathbf{k}) & -\Delta/2 \end{pmatrix},$$

$$\hat{S}_1 = \begin{pmatrix} 1 & s_0 f(\mathbf{k}) \\ s_0 f^*(\mathbf{k}) & 1 \end{pmatrix},$$

$$f(\mathbf{k}) = e^{ik_y a/\sqrt{3}} + 2e^{-ik_y a/2\sqrt{3}} \cos(k_x a/2).$$

Here, the parameter γ_0 describes the strength of nearest-neighbor hopping that yields the Fermi velocity $v = (\sqrt{3}/2) a\gamma_0/\hbar$,[41] and a is the lattice constant. The parameter $s_0 \ll 1$ describes the nonorthogonality of orbitals and $\Delta = \epsilon_A - \epsilon_B$ describes a possible asymmetry between A and B sites (thus opening a gap $|\Delta|$). Here, note that we neglected next-nearest-neighbor hops, which do not produce any visible change in the calculated spectra. The angular dependence of $f(\mathbf{k})$ (on angle φ, which is the angle of the wave vector measured from the center of the valley) is called trigonal warping because the form of the Fermi line around the center of the valley is slightly deformed. This deformation increases with an increase in the absolute value of the wave vector.

Figure 1(d) shows the constant-energy intensity patterns ("maps") at 1.45 eV below the charge-neutrality point[38] in monolayer graphene, which are plotted as a function of photoelectron wave vector $\mathbf{p}_\parallel = (p_x, p_y)$ parallel to the surface of

graphene, covering the whole Brillouin zone. Since the patterns in the vicinity of each Brillouin zone corner are the same but rotated with respect to each other, we describe what is happening around one Brillouin zone corner in detail. Figure 2(b) shows a series of plots demonstrating the evolution of the constant-energy map with energy for the valley $\mathbf{K}_+ = (4\pi/3a, 0)$. Each plot is for a different fixed energy from the charge-neutrality point with energies above (below) on the left- (right-) hand side. For states above the charge-neutrality point (left), the angular variation is $\cos^2(\varphi/2)$, where φ is the angle of the momentum measured from the center of the valley: a comparison to Eq. (3) yields $\phi \equiv \varphi$, illustrating that the isospin is parallel to the momentum $\sigma \cdot \mathbf{n}_1 = 1$. Figure 2(b) (right) shows the intensity for emission from states below the charge-neutrality point in monolayer graphene. In this case, the patterns are flipped with respect to those of the left and the comparison to Eq. (3) yields $\phi = \varphi + \pi$, indicating that the isospin is antiparallel to the momentum $\sigma \cdot \mathbf{n}_1 = -1$.

Figure 2(c) shows the development of the fixed-energy intensity pattern as the asymmetry of on-site lattice energies $\Delta = \epsilon_A - \epsilon_B$ increases, opening a small gap in the spectrum. There are two principal effects on the ARPES spectrum. For energy gaps $|\Delta|/2 \ll |\epsilon|$, the mixing of the wave functions between A and B sites destroys the perfect cancellation of the ARPES intensity so that the ratio between the maximum and minimum intensity becomes finite [Fig. 2(c), left image]. As the gap increases toward the probed energy, the ARPES contour becomes smaller and the intensity anisotropy vanishes [Fig. 2(c), middle and right]. Thus, the opening of an AB asymmetry gap in the monolayer spectrum is accompanied by the loss of the chirality-related anisotropy of ARPES angular maps at low energies, which can be used not only as a strong test for the symmetry-breaking effect induced by a SiC substrate[18] but also as a probe of wave function mixing by AB asymmetry or trigonal warping. Unlike AB asymmetry, whose effects on the ARPES intensity are strongest near the charge-neutrality point, trigonal warping affects the ARPES spectral intensity only at very large energies.

For finite Δ, an analytical, approximate description of the ARPES intensity can be developed as follows: By expressing the wave vector $\mathbf{k} = \mathbf{K}_\pm + \mathbf{q}$ in terms of the wave vector $\mathbf{q}$ measured from the center of the valley $K_\pm$, for electronic energies much less than the π-band width ($qa \ll 1$), the function $f(\mathbf{k})$ may be written as

$$f(\mathbf{k}) \approx -\frac{\sqrt{3}a}{2}(q_x - iq_y) + \frac{a^2}{8}(q_x + iq_y)^2 \tag{5}$$

and

$$\hat{\mathcal{H}}_1 \approx \begin{pmatrix} \Delta/2 & v\pi^\dagger - \mu(\pi)^2 \\ v\pi - \mu(\pi^\dagger)^2 & -\Delta/2 \end{pmatrix}, \quad \pi = \hbar q_x + i\hbar q_y,$$

where $\mu = \gamma_0 a^2/8\hbar^2$ describes the strength of trigonal warping (we assume that $\mu\hbar q \ll v$). This determines the spectrum

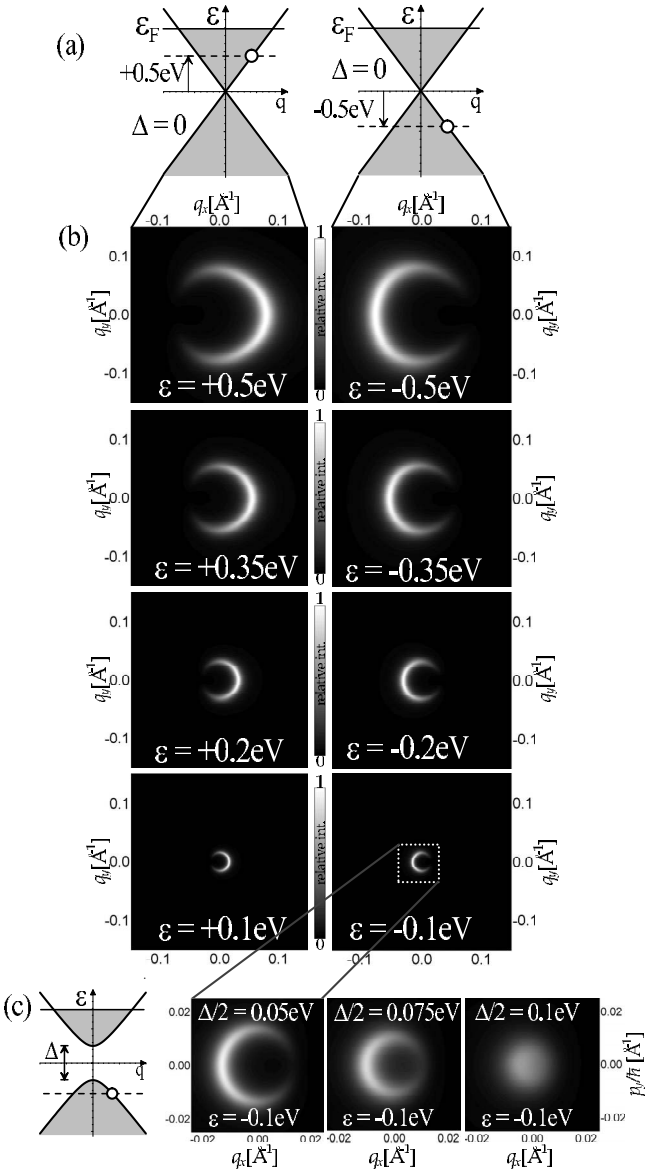

FIG. 2. (a) Schematics of the low-energy bands $\epsilon = \pm\hbar v q$ near the K_+ point in the absence of intralayer asymmetry Δ. (b) The intensity of photoemission from states at a fixed energy close to the charge-neutrality point in monolayer graphene, which is plotted as a function of photoelectron wave vector $\mathbf{q}_\parallel = (q_x, q_y)$ parallel to the surface of graphene in the vicinity of valley $\mathbf{p}_\parallel = (4\pi/3a, 0)$. Each plot corresponds to a different energy with respect to the charge-neutrality point either above (left-hand side) or below (right-hand side). The units of relative intensity (from 0 to 1) are chosen to illustrate the anisotropy, with different integral intensities in different rows. The parameter values are $\gamma_0 = 3.0$ eV, $s_0 = 0.129$, and $\Delta = 0$, and the energy width Γ varies as the energy is divided by 6. (c) The development of the intensity pattern for emission at a fixed energy of 0.1 eV below the charge-neutrality point in the vicinity of valley $\mathbf{p}_\parallel = (4\pi/3a, 0)$ in monolayer graphene as intralayer asymmetry increases in magnitude as $\Delta/2 = 0.05$, 0.075, and 0.1 eV. The parameter values are $\gamma_0 = 3.0$ eV and $s_0 = 0.129$, and the Lorentzian energy broadening is $\Gamma = 0.0167$.

$$\epsilon_q \approx s\sqrt{\hbar^2 v^2 q^2 - 2\xi\mu v\hbar^3 q^3 \cos 3\varphi + \mu^2\hbar^4 q^4 + \frac{\Delta^2}{4}}, \quad (6)$$

where $s=1$ ($s=-1$) stands for the conduction (valence) band index and leads to the ARPES angular-dependent intensity by using Eq. (4),

$$I \sim |\Phi_{\mathbf{p}}|^2\left\{1 + \left|\frac{\hbar v q}{\epsilon_q}\right|\left[\cos(2\theta) - \frac{\xi\mu\hbar q}{v}\cos(2\theta - 3\xi\varphi)\right]\right\} \times \delta(E_{\mathbf{p}} + A - \epsilon_q - \hbar\omega)\,\delta_{\mathbf{q},\mathbf{p}_\parallel - \mathbf{K}_\pm - \mathbf{G}}, \quad (7)$$

where $\theta = \frac{\xi\varphi}{2} - \frac{\pi}{3}(m_1 - m_2) + \frac{\pi}{4}(1 - s\xi)$. Equations (6) and (7) contain the full dependence on valley $\xi = \pm 1$ and reciprocal lattice vector (m_1, m_2) indices.[42]

III. PHOTOEMISSION FROM BILAYER GRAPHENE

A. Use of angle-resolved photoelectron spectroscopy to determine the sign of interlayer coupling parameter γ_1

Bilayer graphene[4,5,26] consists of two coupled hexagonal lattices with inequivalent sites $A1, B1$ and $A2, B2$ in the first and second graphene sheets, respectively, which are arranged according to Bernal ($A2$-$B1$) stacking,[26] as shown in Fig. 3(a). As in the monolayer, the Brillouin zone has two inequivalent degeneracy points $K_\pm$, which determine two valleys centered on zero energy in the electron spectrum. Near the center of each valley, the electron spectrum consists of four branches [Fig. 3(b)], with two branches describing states on sublattices $A2$ and $B1$ that are split from zero energy by about $\pm|\gamma_1|$, which is determined by the interlayer coupling γ_1, whereas two low-energy branches are formed by states based on sublattices $A1$ and $B2$. The anisotropy of ARPES for a twin bilayer crystal with $B2$-$A1$ stacking is discussed in Ref. 50.

To model bilayer graphene, we use a tight-binding Hamiltonian matrix $\hat{H}_2$ and an overlap-integral matrix $\hat{S}_2$ that operate in the space of coefficients $\psi^T = (\psi_{A1}, \psi_{B2}, \psi_{A2}, \psi_{B1})$ at valley K_+,[26,27,43]

$$\hat{H}_2 = \begin{pmatrix} \epsilon_{A1} & \gamma_3 f^*(\mathbf{k}) & \gamma_4 f(\mathbf{k}) & -\gamma_0 f(\mathbf{k}) \\ \gamma_3 f(\mathbf{k}) & \epsilon_{B2} & -\gamma_0 f^*(\mathbf{k}) & \gamma_4 f^*(\mathbf{k}) \\ \gamma_4 f^*(\mathbf{k}) & -\gamma_0 f(\mathbf{k}) & \epsilon_{A2} & \gamma_1 \\ -\gamma_0 f^*(\mathbf{k}) & \gamma_4 f(\mathbf{k}) & \gamma_1 & \epsilon_{B1} \end{pmatrix},$$

$$\hat{S}_2 = \begin{pmatrix} 1 & 0 & 0 & s_0 f(\mathbf{k}) \\ 0 & 1 & s_0 f^*(\mathbf{k}) & 0 \\ 0 & s_0 f(\mathbf{k}) & 1 & s_1 \\ s_0 f^*(\mathbf{k}) & 0 & s_1 & 1 \end{pmatrix}. \quad (8)$$

We adopt the notation of the Slonczewski–Weiss–McClure model[10,11] that is often used to describe bulk graphite in order to parametrize the couplings relevant to bilayer graphene.[41] Nearest-neighbor coupling within each plane is parametrized by coupling γ_0 [$v = (\sqrt{3}/2)a\gamma_0/\hbar$] and interlayer $A2$-$B1$ coupling is described by γ_1. The parameter γ_3 describes direct $A1$-$B2$ interlayer coupling, which leads to an effective velocity $v_3 = -(\sqrt{3}/2)a\gamma_3/\hbar$ that represents the magnitude of trigonal warping, which is particularly relevant at low energy [we assume that $\hbar v q \gg |\gamma_1(v_3/v)|$].

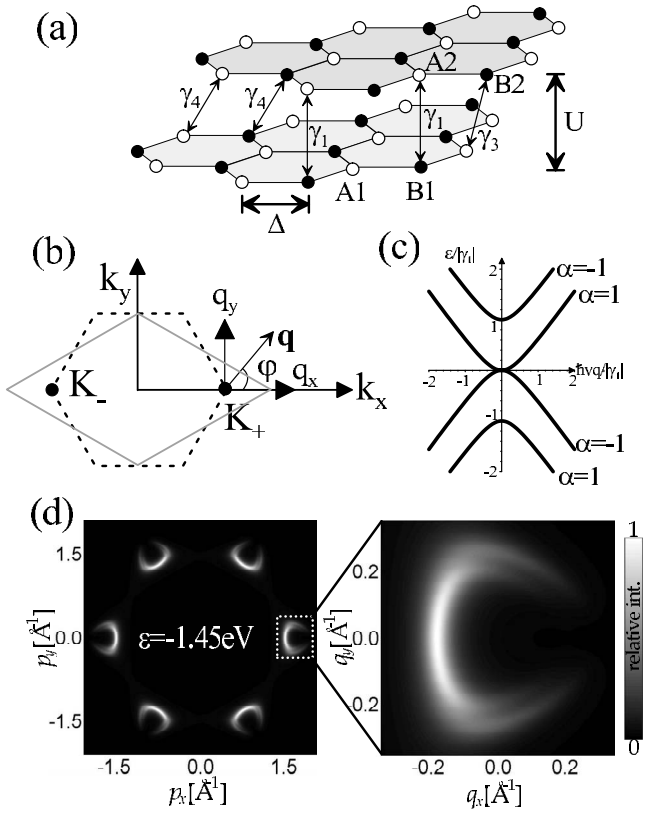

FIG. 3. (a) Schematic of the bilayer lattice containing four sites in the unit cell: $A1$ (white circles) and $B1$ (black circles) at the bottom layer and $A2$ (white circles) and $B2$ (black circles) at the top layer. (b) Schematic of the hexagonal and rhombic Brillouin zone indicating two inequivalent valleys $K_\pm$ showing the wave vector $\mathbf{q} = (q\cos\varphi, q\sin\varphi)$ measured from the center of valley K_+. (c) Schematic of the low energy bands in the absence of lattice asymmetry. The energy band index $\alpha = \pm 1$ [Eq. (11)] is explicitly shown for the case $\gamma_1 < 0$. (d) The intensity of photoemission from states at a constant energy of 1.45 eV below the charge-neutrality point in bilayer graphene, which is plotted as a function of photoelectron wave vector $\mathbf{p}_\parallel = (p_x, p_y)$ parallel to the surface of graphene for $\mathbf{p}_\parallel$ covering the whole Brillouin zone (left) and plotted as a function of photoelectron wave vector $\mathbf{q} = (q_x, q_y)$ in the vicinity of valley K_+ (right) (note that the origin and scale of $\mathbf{p}_\parallel$ and $\mathbf{q}$ are different). Here, we use the parameter values $\gamma_0 = 3.0$ eV, $\gamma_1 = -0.35$ eV, $\gamma_3 = -0.15$ eV, $\gamma_4 = 0.0$ eV, $s_0 = 0.129$, and $\Delta = U = 0$, and energy width $\Gamma = 0.24$ eV.

The parameter γ_4 describes $A1$-$A2$ and $B1$-$B2$ interlayer hoppings. We studied its influence on the intensity pattern for emission at a fixed energy of 0.1 eV below the charge-neutrality point in bilayer graphene (as in Figs. 7–9) and found no noticeable effect for values $\gamma_4 \lesssim 0.1$ eV. For simplicity, we use $\gamma_4 = 0$ throughout. Note that a magnetoreflection study of graphite measured $\gamma_4 = 0.044$ eV,[44] whereas a recent Raman scattering experiment on bilayer graphene found $\gamma_4 = 0.12$ eV.[45] The parameter $s_0 \ll 1$ describes the nonorthogonality of orbitals on the same layer. Following numerical analysis, we found no noticeable effect for values $s_0 \lesssim 0.2$ on the intensity pattern for emission at a fixed energy

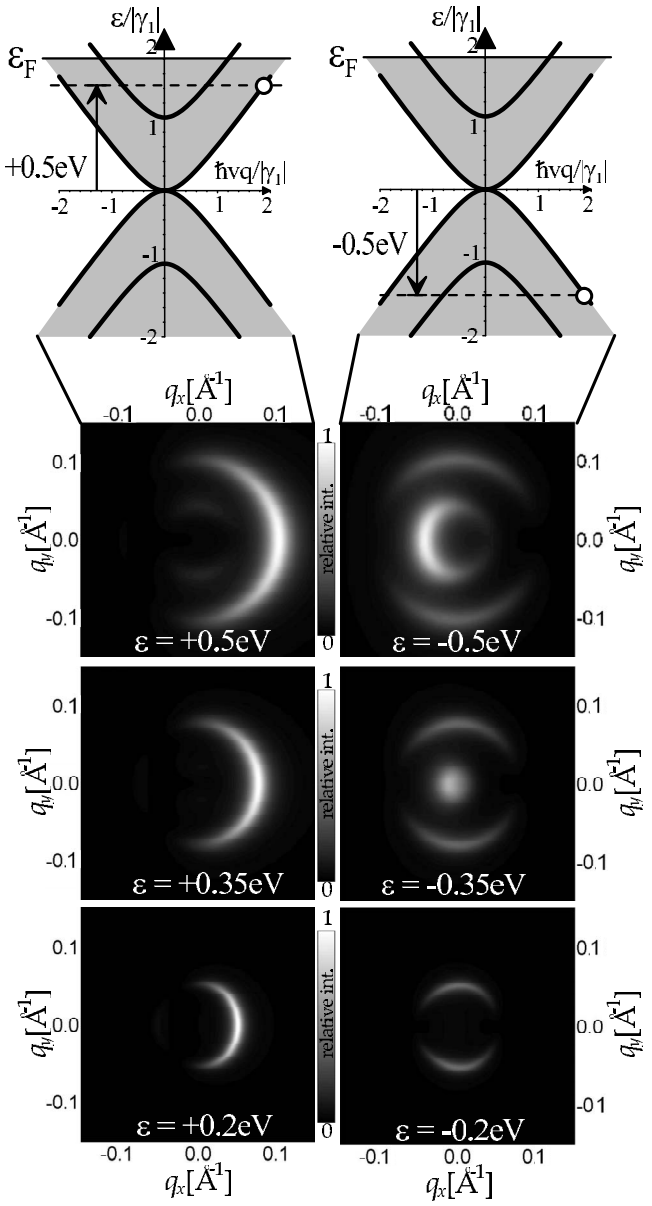

FIG. 4. The intensity of photoemission from states at a fixed energy close to the charge-neutrality point in bilayer graphene, which is plotted as a function of photoelectron wave vector $\mathbf{q}=(q_x,q_y)$ parallel to the surface of graphene in the vicinity of valley $\mathbf{p}_\parallel=(4\pi/3a,0)$. Each plot corresponds to a different energy with respect to the charge-neutrality point either above (left) or below (right). Units of relative intensity (from 0 to 1) are chosen to illustrate the anisotropy, with different integral intensities in different rows. The parameter values are $\gamma_0=3.0$ eV, $\gamma_1=-0.35$ eV, $\gamma_3=-0.15$ eV, $\gamma_4=0.0$ eV, $s_0=0.129$, and $\Delta=U=0$, and the energy width Γ varies as the energy is divided by 6.

of 0.1 eV below the charge-neutrality point in bilayer graphene. Throughout the paper, we use $s_0=0.129$.[39] The parameter s_1 describes nonorthogonality terms arising from overlaps between orbitals on different layers. We found no noticeable effect for values $s_1 \lesssim 0.1$ on the intensity pattern for emission at a fixed energy of 0.1 eV below the charge-neutrality point in the bilayer graphene, and in the following angular maps, we use $s_1=0$. Other weaker tunneling processes, including the next-nearest-neighbor hopping, are also neglected. We note that some works on bilayer graphene use different definitions of the tight-binding parameters (for example, γ_3 is defined with an additional minus sign in Refs. 26, 31, and 33, but it has no effect on their conclusions).

The Bloch function amplitudes $\psi^T=(\psi_{A1},\psi_{B2},\psi_{A2},\psi_{B1})$ and band energy $\epsilon_{\mathbf{q}}$, which are found using the Hamiltonian [Eq. (8)], can be used to model the photoemission intensity. In this section we consider the limit of small photon energy such that $p_z d \ll 1$ (where d is the interlayer spacing of bilayer graphene). Figure 3(c) shows constant-energy maps at 1.45 eV below the charge-neutrality point[38] in bilayer graphene, with the plot on the left-hand side showing values of $\mathbf{p}_\parallel$ covering the whole Brillouin zone. The patterns in each valley are the same but rotated with respect to the others so that we can focus on one of them [highlighted in Fig. 3(c)]. The anisotropy of the bilayer pattern at this energy is similar to that of the monolayer [Fig. 1(d)] because the energetic width $\Gamma \sim |\gamma_1|$ obscures features associated with the presence of two bands. To observe differences between the two materials, we need to consider the ARPES patterns at energies closer to the charge-neutrality point.

Figure 4 illustrates the evolution of the intensity pattern with energy. At energies greater than the interlayer coupling, i.e., $|\epsilon_q| > |\gamma_1|$ (the top two patterns), there are two ringlike patterns, each corresponding to photoemission from states in two bands, whereas for low energies, i.e., $|\epsilon_q| < |\gamma_1|$ (the bottom two patterns), there is a single ring corresponding to emission from the degenerate band only. Although these plots have been obtained by using a complete bilayer Hamiltonian [Eq. (8)], it is convenient to discuss salient features of the results in Fig. 4 by using an analytic formula, which is obtained by performing a linear-in-momentum expansion of $f(\mathbf{k})$ [Eq. (5)] and neglecting trigonal warping due to $A1$-$B2$ interlayer coupling ($\gamma_3=0$), $A1$-$A2$ and $B1$-$B2$ interlayer couplings ($\gamma_4=0$), and the nonorthogonality of orbitals ($s_1=s_0=0$). In this case, the four bands in the bilayer spectrum are described by

$$\epsilon_q \approx s\frac{1}{2}|\gamma_1|[\sqrt{1+4\hbar^2 v^2 q^2/\gamma_1^2}+b], \tag{9}$$

where the parameters

$$b=\pm 1, \quad s=\pm 1$$

identify the four bands: $b=1$ for the split bands with energy $|\epsilon_q| \geq |\gamma_1|$ and $b=-1$ for the low-energy "degenerate" bands that touch at zero energy, while $s=1$ ($s=-1$) indicates the conduction (valence) bands. Then, the contribution of a given band is

$$I \sim \frac{|\Phi_{\mathbf{p}}|^2 g(\varphi)}{[1+(\epsilon_q/\hbar v q)^2]}\delta(E_{\mathbf{p}}+A-\epsilon_q-\hbar\omega)\delta_{\mathbf{q},\mathbf{p}_\parallel-\mathbf{K}_\pm-\mathbf{G}},$$

where

$$g(\varphi) = \frac{1}{2}\left| e^{-i\varphi} + \alpha e^{i\varphi} + \frac{\epsilon_q}{\hbar v q}(\alpha+1)\right|^2$$
$$= 1 + \alpha\cos(2\varphi) + \delta_{\alpha,1}\left[\frac{4\epsilon_q}{\hbar v q}\cos(\varphi) + 2\left(\frac{\epsilon_q}{\hbar v q}\right)^2\right] \quad (10)$$

and

$$\alpha = sb\gamma_1/|\gamma_1|. \quad (11)$$

As the value of α [Eq. (11)] depends on the sign of the tight-binding parameter γ_1, a comparison of the angular dependence of $g(\varphi)$ to experimental data provides a method to determine the sign of γ_1.[41] To demonstrate this, we make a comparison to our numerical data, which are plotted in Fig. 4. In this illustration, we assume that $\gamma_1<0$, which is a natural choice given the $z\to -z$ asymmetry of the p_z orbitals of carbon. This choice of the sign of γ_1 shows how the anisotropies of photoemission angular maps differ in the split bands and degenerate bands at energies above, $\epsilon>0$, and below, $\epsilon<0$, the charge neutrality point. Note that changing the sign of γ_1 to positive would lead to an interchange of plots, illustrating the ARPES behavior at $\epsilon>0$ and $\epsilon<0$.

The most pronounced feature of the ARPES angular maps, which are depicted for $\gamma_1<0$ in Fig. 4, is that for energies $\epsilon>0$ (left side of Fig. 4), photoemission spectra are dominated by states in the degenerate bands, $b=-1$, which are nicely described by the intensity profile $I\propto\cos^2\varphi/2$. In contrast, for $\epsilon<0$ (valence bands, right-hand side of Fig. 4), ARPES intensity from the degenerate band $b=-1$ is weak, whereas the split band, which is at energies $\epsilon<-|\gamma_1|$, produces a bright dominant signal. If experimentally observed, such behavior of ARPES maps in the conduction and valence bands would be indicative of a negative sign of the interlayer coupling γ_1.[41] If the experimentally observed constant-energy maps were interchanged for negative and positive energies, these would be evidence for $\gamma_1>0$. Although the sign of γ_1 has directly observable consequences for the ARPES pattern, tight-binding parameters for graphite published so far have assumed that $\gamma_1>0$ (see Ref. 46, and references therein).

B. Electron chirality in the angle-resolved photoelectron spectroscopy of bilayer graphene and the use of trigonal warping to determine the sign of the interlayer coupling γ_3

The behavior of low-energy particles in bilayer graphene is perhaps even more remarkable[4,5,26] than that in monolayer graphene. The low-energy bands (at energy $|\epsilon|\ll|\gamma_1|$) have a parabolic energy versus momentum relation and they support eigenstates of an operator $\sigma\cdot\mathbf{n}_2$ with $\sigma\cdot\mathbf{n}_2=1$ for electrons in the conduction band and $\sigma\cdot\mathbf{n}_2=-1$ for electrons in the valence band, where $\mathbf{n}_2(\mathbf{q})=[\cos(2\varphi),\sin(2\varphi)]$, which means that they are chiral, but with a degree of chirality that is different from that in the monolayer graphene, with the isospin linked to, but turning twice as quickly as, the direction of momentum. An interpretation of the ARPES constant-energy maps in terms of two-source interference [Eq. (3)] predicts an angular variation, such as $\cos^2(\varphi)$ for states above the charge-neutrality point and $\cos^2(\varphi+\pi/2)$ for states below (for $\gamma_1<0$).

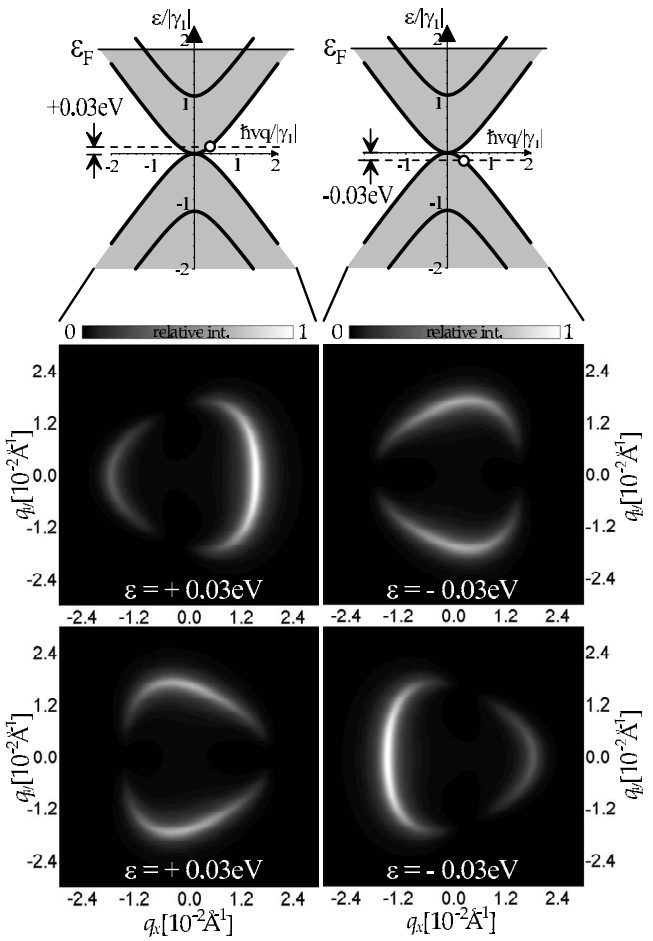

FIG. 5. The intensity of photoemission in bilayer graphene for fixed energy very close to the charge-neutrality point in the vicinity of valley $\mathbf{p}_\parallel=(4\pi/3a,0)$: for states with an energy of 0.03 eV above the charge-neutrality point (left) and states with an energy of 0.03 eV below the charge-neutrality point (right). We consider different signs of the $A2$-$B1$ interlayer coupling strength γ_1, with $\gamma_1=-0.35$ eV (top) and $\gamma_1=+0.35$ eV (bottom). The other parameter values are $\gamma_0=3.0$ eV, $\gamma_3=-0.15$ eV, $\gamma_4=0.0$ eV, $\Gamma=0.005$ eV, and $s_0=0.129$ (Ref. 39).

Figure 5 shows the calculated intensity of the photoemission in the vicinity of valley $\mathbf{p}_\parallel=(4\pi/3a,0)$ from states very close to the charge-neutrality point in the bilayer graphene at energies of 0.03 eV above (left-hand side) and 0.03 eV below (right-hand side). We consider two different signs of the $A2$-$B1$ interlayer coupling strength γ_1, with $\gamma_1=-0.35$ eV (top) and $\gamma_1=+0.35$ eV (bottom). For $\gamma_1<0$ and emission from the valence band (top right), the pattern is similar to $\cos^2(\varphi+\pi/2)$ as expected for the two-source interference of chiral electron in the bilayer graphene. As shown in Eq. (10) (and explained in detail in Sec. IV), the intensity from this band is not affected by corrections due to the presence of dimer $A2$-$B1$ orbitals (it has $\alpha=-1$). For emission from the conduction band (top left side of Fig. 5), the interference pattern has two peaks, but one of the peaks has about three times stronger maximum intensity than the other because of

the presence of the contribution from dimer $A2$-$B1$ orbitals (this band has $\alpha=+1$).[47] The bottom-left and bottom-right plots in Fig. 5 show the constant-energy maps for $\gamma_1>0$ for emission above and below the charge-neutrality point, respectively. In this case, the intensity pattern for emission from the conduction band (bottom left) has two peaks with the same maximum intensity, which arises from the interference of waves from the $A1$ and $B2$ sublattices. For emission from the valence band (bottom right), the peaks have different maximum intensities, owing to the interference of waves from four sublattices.

We note that once the sign of γ_1 is known, the sign of $A1$-$B2$ interlayer coupling γ_3 may also be deduced from the orientation of trigonal warping of the intensity patterns near the charge-neutrality point.[41] In the bilayer graphene, there are two principal causes of trigonal warping. The first is the presence of $A1$-$B2$ interlayer coupling γ_3 that will tend to dominate at low energy and the second is the higher-in-momentum terms in the function $f(\mathbf{k})$ that will be important at large energies. The latter causes trigonal warping in the monolayer graphene, while the former is not present in the monolayer graphene. At large energies, when the higher-in-momentum terms dominate, the orientation of trigonal warping in the bilayer graphene [e.g., Fig. 3(c)] is the same as that in the monolayer graphene [e.g., Fig. 1(d)], whereas at low energies, the orientation of trigonal warping in the bilayer graphene depends on the sign of parameter γ_3 (assuming that the sign of γ_1 is known).

The orientation of trigonal warping flips on changing the sign of γ_1, as seen by comparing the top and bottom plots in Fig. 5. At very low energies, $\epsilon_q, \hbar v q \ll |\gamma_1|$, and in the absence of lattice asymmetry, the energy eigenvalues[26] are

$$\epsilon_q \approx \pm \sqrt{\hbar^2 v_3^2 q^2 - 2\xi \frac{v_3 v^2 \hbar^3 q^3}{\gamma_1} \cos 3\varphi + \frac{\hbar^4 v^4 q^4}{\gamma_1^2}}, \quad (12)$$

where $v_3=-(\sqrt{3}/2)a\gamma_3/\hbar$. This expression illustrates that the angular dependent factor, which produces trigonal warping, depends on the sign of the ratio γ_3/γ_1. In this paper, we usually choose $\gamma_1<0$ and $\gamma_3<0$ to illustrate the possibility that the orientation of trigonal warping is different at lower energies [e.g., Fig. 5 (top)] from that at higher energies.

C. Substrate-induced asymmetry in bilayer graphene

The Hamiltonian $\hat{H}_2$ [Eq. (8)] takes into account the possibility of different on-site energies through its diagonal components. Their effect may be understood by considering the eigenenergies to be exactly at the center of the valley, where $f(\mathbf{k})=0$, namely, $\epsilon=\epsilon_{A1}$, $\epsilon=\epsilon_{B2}$, or

$$\epsilon = \frac{1}{2}(\epsilon_{A2}+\epsilon_{B1}) \pm \sqrt{\frac{1}{4}(\epsilon_{A2}-\epsilon_{B1})^2+\gamma_1^2}.$$

Below, we distinguish between two types of asymmetry in the bilayer graphene[50] parametrized by using $\Delta=\epsilon_{A1}-\epsilon_{B1}$, which is the difference between on-site energies of adjacent atoms at the bottom layer due to the presence of a substrate, and interlayer asymmetry $U=[(\epsilon_{A1}+\epsilon_{B1})-(\epsilon_{A2}+\epsilon_{B2})]/2$ between on-site energies in the two layers arising from a doping effect and charge transfer to the substrate.[5,7,8,26–34]

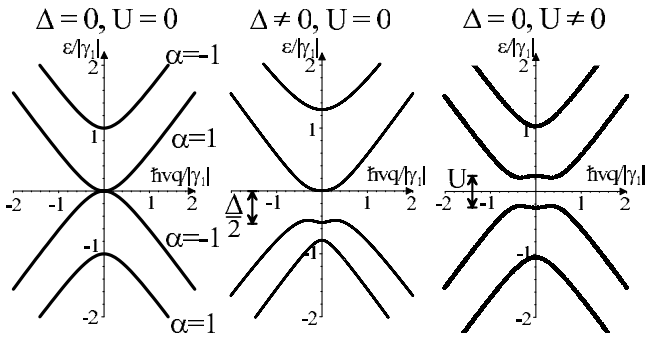

FIG. 6. The band structure of bilayer graphene in the vicinity of a valley for no lattice asymmetry (left), substrate-induced asymmetry $\Delta=\gamma_1<0$ ($U=0$) (center), and interlayer asymmetry $U=\gamma_1/2$ ($\Delta=0$) (right). For clarity, we use large values of asymmetry. The energy band index $\alpha=\pm 1$ [Eq. (11)] is explicitly shown for the case $\gamma_1<0$ on the left-hand side.

In Fig. 6 (center), the band structure in the vicinity of the K point is plotted in the presence of a substrate-induced asymmetry $\Delta=\epsilon_{A1}-\epsilon_{B1}$ [the plot is shown for $\gamma_1<0$ and $\Delta<0$]. This type of asymmetry introduces a gap $\sim|\Delta|/2$ as well as an electron-hole asymmetry. In Fig. 6 (right), the band structure in the vicinity of the K point is plotted in the presence of an interlayer asymmetry $U=[(\epsilon_{A1}+\epsilon_{B1})-(\epsilon_{A2}+\epsilon_{B2})]/2$. It does not break electron-hole symmetry but introduces a gap $\sim|U|$.

As illustrated in Fig. 7, the constant-energy maps are sensitive both to the magnitude and sign of the asymmetry Δ. The plots on the left- (right-) hand side of Fig. 7 show constant-energy maps for photoemission from conduction (valence) band states at an energy of 0.1 eV above (below) the midgap energy. The top two plots are for no asymmetry $\Delta=0$, the middle two plots show negative asymmetry $\Delta/2=-0.15$ eV, and the bottom two show positive asymmetry $\Delta/2=+0.15$ eV. As for the monolayer, one effect of asymmetry Δ is to impair the two-source interference, resulting in a weakening of the angular anisotropy of the intensity pattern. The "Mexican hat" structure (also known as a "camelback" in Te and GaP literature[48,49]) of the valence band for negative Δ and the conduction band for positive Δ is manifested in the larger ARPES contour for emission from these states (shown in the middle right and the bottom left, respectively) as opposed to their counterparts in the other bands (middle left and bottom right, respectively). Experimentally, such a difference in the size and nature of the ARPES contour for emission from conduction or valence bands (at the same distance from the midgap energy) would indicate the presence and sign of intralayer asymmetry Δ.

Since interlayer asymmetry U results in a gap $\sim|U|$ that preserves electron-hole symmetry and does not depend on the sign of U, the constant-energy photoemission maps are sensitive to the magnitude of U but not its sign. Figure 8 shows the constant-energy maps for photoemission from conduction band states at an energy of 0.1 eV above the charge-neutrality point (left-hand side) and from valence band states at an energy of 0.1 eV below the charge-neutrality point (right-hand side) as U increases in magni-

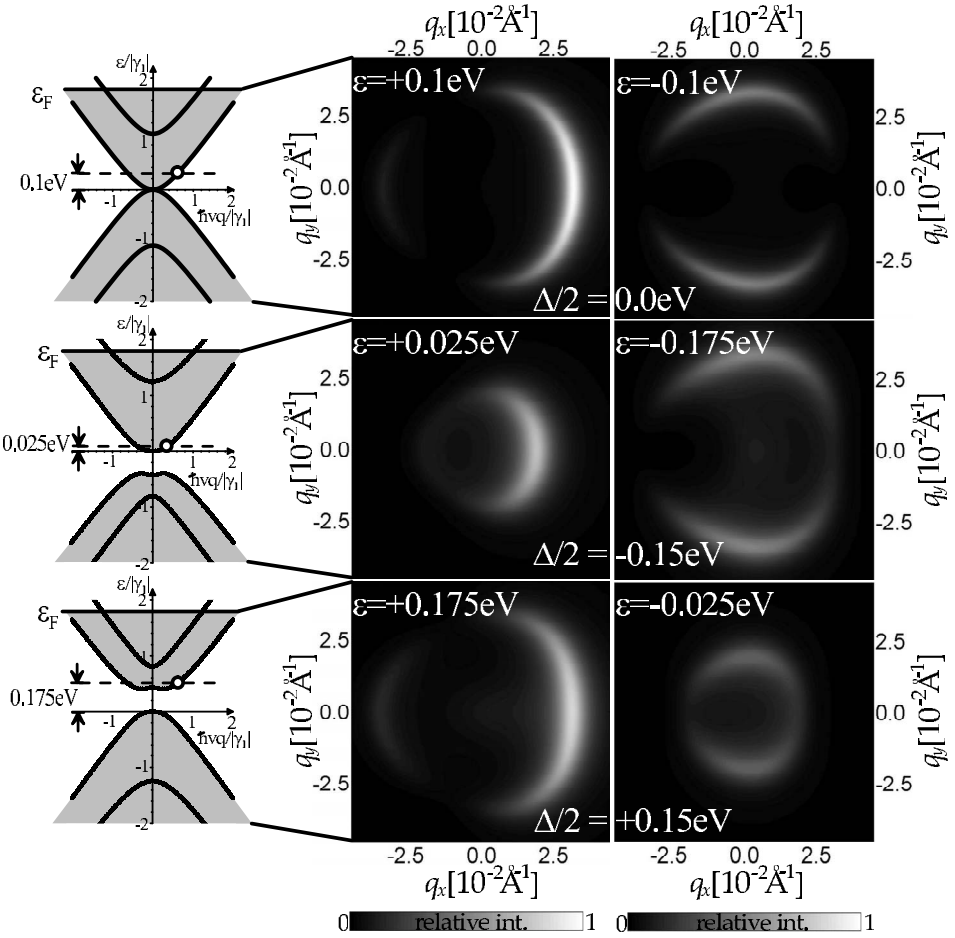

FIG. 7. Left (right) shows the development of the intensity pattern for emission at a fixed energy of 0.1 eV above (below) the midgap energy in bilayer graphene in the vicinity of valley $\mathbf{p}_{\parallel}=(4\pi/3a,0)$ as intralayer asymmetry $|\Delta|$ increases [the energy with respect to the charge-neutrality point is also indicated]. The plots show $\Delta=0$ (top), negative $\Delta/2=-0.15$ eV (middle), and positive $\Delta/2=0.15$ eV (bottom). The same scale of relative intensity (from 0 to 1) is used in all graphs. The parameter values are $\gamma_0=3.0$ eV, $\gamma_1=-0.35$ eV, $\gamma_3=-0.15$ eV, $\gamma_4=0.0$ eV, $s_0=0.129$, and $\Gamma=0.0167$ eV.

tude. Generally, the effect of asymmetry U is to weaken the angular anisotropy of the intensity pattern. Both the conduction and valence bands in the vicinity of the charge neutrality point display a Mexican hat structure,[26–28] leading to relatively large ARPES contours (and additional features, as seen in the plot at $U/2=0.1$ eV), which is in contrast to asymmetry Δ (Fig. 7) where the Mexican hat structure appears in one band only.

D. Dependence of the interference of photoelectrons emitted from bilayer sublattices on the incident photon energy

Our numerical data for bilayer graphene (Figs. 4 and 5) show that the anisotropy of photoemission angular-maps differs in the split bands and degenerate bands at energies above $\epsilon>0$ (left side of Fig. 4) and below $\epsilon<0$ (right side of Fig. 4) the charge-neutrality point. These plots may be interpreted in terms of the interference of photoelectron waves emitted from four nonequivalent sublattices. In fact, for two of the four bands, the parameter $\alpha=-1$ in Eq. (10) so that the contribution of orbitals on the "dimer" $A2$ and $B1$ sites cancel, leaving only the contribution of two terms $e^{\pm i\varphi}$ in $g(\varphi)$ that arise from orbitals on the $A1$ and $B2$ sites. For the other two bands, i.e., $\alpha=1$, the contribution of orbitals on the dimer $A2$ and $B1$ sites to $g(\varphi)$ do not cancel but interfere with the contribution of orbitals on $A1$ and $B2$ sites, producing a different angular dependence and a greater peak intensity than those for $\alpha=-1$.

As the value of α [Eq. (11)] depends on the sign of γ_1, a comparison of the angular dependence of $g(\varphi)$ to experimental data provides a method to determine the sign of γ_1.[41] To demonstrate this, we make a comparison to our numerical data, which are plotted in Fig. 4. For the sign of γ_1 that we adopt in the numerics ($\gamma_1<0$), the split band above the charge-neutrality point has $\alpha=-1$, so the intensity from this band appears as a very faint ring (that of smaller radius) in the plot at energy $\epsilon=+0.5$ eV in Fig. 4. The degenerate band at this energy, however, has $\alpha=1$ so the intensity from it appears as a ring of larger radius with a larger peak intensity. As the energy drops below $|\gamma_1|$ (left side of Fig. 4) the contribution of the split band disappears to leave only the ring arising from the degenerate band with $\alpha=1$. The energy has to approach the charge-neutrality point before the contribution of the dimer $A2$ and $B1$ sites, which are small in the parameter $\epsilon_q/\hbar vq\approx\sqrt{\epsilon_q/\gamma_1}$, weakens to reveal an anisotropy pattern characteristic of a two-source interference in bilayer graphene, as explained in Sec. III B.[47]

The picture is quite different for energies below the charge-neutrality point (right side of Fig. 4). In this case, the split band has $\alpha=1$, so the intensity from it appears as the ring (of smaller radius) with a larger peak intensity at energy $\epsilon=-0.5$ eV in Fig. 4. The degenerate band has $\alpha=-1$, so the intensity from it appears as the fainter ring (that of a larger

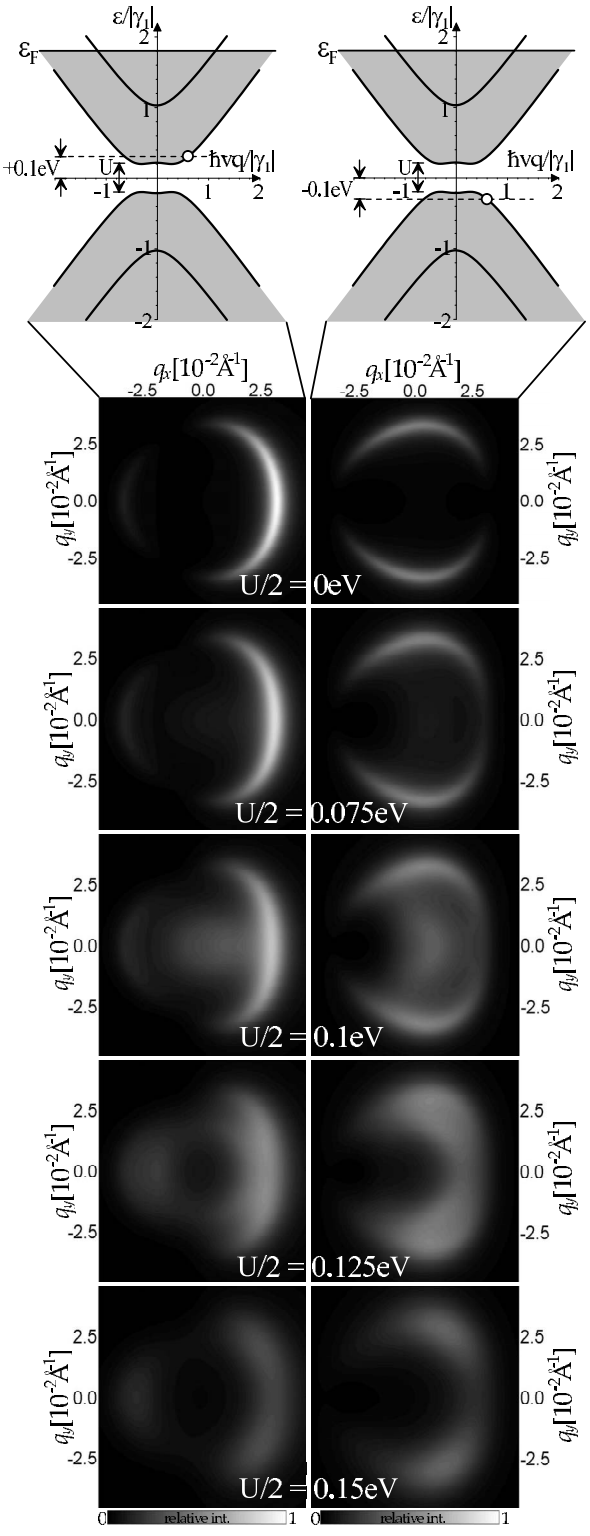

FIG. 8. The development of the intensity pattern in bilayer graphene in the vicinity of valley $\mathbf{p}_{\|}=(4\pi/3a,0)$ as interlayer asymmetry $U/2=0$, 0.075, 0.1, 0.125, and 0.15 eV increases for emission from states with an energy of 0.1 eV above the charge-neutrality point on the left-hand side and an energy of 0.1 eV below the charge-neutrality point on the right-hand side. The same scale of relative intensity (from 0 to 1) is used in all graphs. The parameter values are $\gamma_0=3.0$ eV, $\gamma_1=-0.35$ eV, $\gamma_3=-0.15$ eV, $\gamma_4=0.0$ eV, $s_0=0.129$, and $\Gamma=0.0167$ eV.

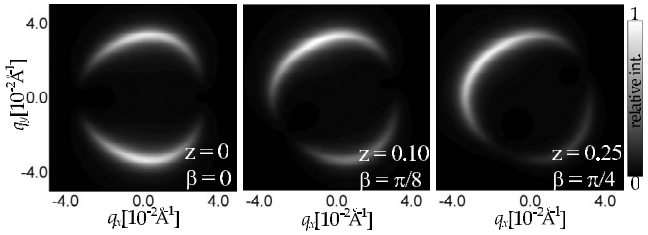

FIG. 9. The development of the intensity pattern in bilayer graphene for emission from states with an energy of 0.1 eV below the charge-neutrality point in the vicinity of valley $\mathbf{p}_{\|}=(4\pi/3a,0)$ as attenuation [described by the factor $\exp(-2z+2i\beta)$, where (z,β) are real parameters] of waves from the bottom layer increases. The parameter values are $\gamma_0=3.0$ eV, $\gamma_1=-0.35$ eV, $\gamma_3=-0.15$ eV, $\gamma_4=0.0$ eV, $s_0=0.129$, and $\Gamma=0.0167$ eV.

radius) at energy $\epsilon=-0.5$ eV. As the energy increases above $-|\gamma_1|$ (right-hand side of Fig. 4), the contribution of the split band disappears to leave only the ring arising from degenerate band with $\alpha=-1$. This is why the intensity pattern $\sim\cos^2(\varphi)$ is much easier to detect below the charge-neutrality point than above it. In fact, whether it is easily visible above or below the charge-neutrality point depends on the sign of γ_1 (here, we chose $\gamma_1<0$), so the experimental observation of the anisotropy $\sim\cos^2(\varphi)$ will provide a way to determine the sign of $A2$-$B1$ interlayer coupling γ_1 in bilayer graphene.

Finally, we note that the anisotropy of the constant-energy maps may be influenced by other factors not modeled here such as the incident photon energy, $\hbar\omega$. For a large value of $\hbar\omega$ the component of photoelectron momentum perpendicular to the bilayer sample p_z is large, so that photoelectron waves emitted from the bottom layer will have a phase shift $\beta=p_z d$ and, possibly, be attenuated with respect to those emitted from the top layer. To obtain an impression of the typical kind of effect, we introduced an exponential factor $\exp(-2z+2i\beta)$ [where (z,β) are real parameters] for waves from the bottom layer. As shown in Fig. 9 for photoemission from states at an energy of 0.1 eV below the charge-neutrality point in bilayer graphene, there is a destruction of the double-peaked intensity pattern and the phase factor β has the effect of rotating the whole pattern.[50]

IV. CONCLUSIONS

Using the Fermi golden rule, we modeled the anisotropy of the intensity of photoemission constant-energy maps at low energy in graphene and demonstrated that the anisotropy is a manifestation of electronic chirality. In monolayer graphene, photoemission may be viewed as a two-source interference experiment, i.e., *à la* Young's double slits; the sources are two inequivalent lattice sites in the unit cell. The resulting intensity $\sim\cos^2(\varphi/2)$ displays a single-peaked dependence on the direction of momentum described by angle φ. In bilayer graphene, the interference of emitted photoelectron waves from four atomic sites produces single- or double-peaked constant-energy maps, which depend on the energy of the initial state in graphene. The marked contrast

between the anisotropy for emission from the conduction or the valence band at energies below the $A2$-$B1$ interlayer coupling strength, which is parametrized by γ_1,[41] provides an experimental method to determine the magnitude and sign of parameter γ_1.

The shape of the photoemission constant-energy maps is determined by the trigonal warping effect in graphene. In monolayers and bilayers, the isoenergetic line changes from an almost circular to a triangularly warped shape as the energy increases: the extent of such warping is controlled by the dimensionless parameter qa, where q is the magnitude of the wave vector measured from the center of the valley and a is the lattice constant. In bilayer graphene, strong trigonal warping may also occur at low energy because of $A1$-$B2$ interlayer coupling, which is parametrized by γ_3,[41] and the observation of this latter trigonal warping provides an experimental method to determine the magnitude and sign of parameter γ_3.

Measurements of the anisotropy of the intensity of photoemission constant-energy maps provide a method to characterize realistic graphene samples. As an example, we take into account the substrate-induced asymmetry that impairs the two-source interference in monolayer graphene, which results in a weakening of the angular anisotropy of the intensity pattern. An analysis of recent experimental data[18,19] in terms of the anisotropy of constant-energy maps may help to shed light on the possible presence of asymmetry in graphene that is epitaxially grown on SiC substrate. In bilayers, both substrate-induced asymmetry and interlayer asymmetry alter the interference pattern: we describe measurable differences between them. This illustrates the potential of photoemission in the future characterization of few-layer graphene samples.

ACKNOWLEDGMENTS

The authors thank B. L. Altshuler, T. Ando, F. Guinea, and A. Lanzara for discussions. This project has been funded by EPSRC-GB Portfolio Partnership EP/C511743/1, by EPSRC-GB First Grant EP/E063519/1, by ESF FoNE project SpiCo EP/D062918/1, by the Royal Society, and by the Daiwa Anglo-Japanese Foundation. The Advanced Light Source is supported by the Director, Office of Science, Office of Basic Energy Sciences, of the U.S. Department of Energy under Contract No. DE-AC02-05CH11231. V.F. also acknowledges support from the Alexander von Humboldt Foundation and hospitality of the University of Hannover.

*Present address: Department of Physics, University of Basel, Klingelbergstrasse 82, 4056 Basel, Switzerland.

[1] K. S. Novoselov, A. K. Geim, S. V. Morozov, D. Jiang, Y. Zhang, S. V. Dubonos, I. V. Grigorieva, and A. A. Firsov, Science **306**, 666 (2004).
[2] K. S. Novoselov, A. K. Geim, S. V. Morozov, D. Jiang, M. I. Katsnelson, I. V. Grigorieva, S. V. Dubonos, and A. A. Firsov, Nature (London) **438**, 197 (2005).
[3] Y. Zhang, Y. W. Tan, H. L. Stormer, and P. Kim, Nature (London) **438**, 201 (2005).
[4] K. S. Novoselov, E. McCann, S. V. Morozov, V. I. Fal'ko, M. I. Katsnelson, U. Zeitler, D. Jiang, F. Schedin, and A. K. Geim, Nat. Phys. **2**, 177 (2006).
[5] T. Ohta, A. Bostwick, T. Seyller, K. Horn, and E. Rotenberg, Science **313**, 951 (2006).
[6] R. V. Gorbachev, F. V. Tikhonenko, A. S. Mayorov, D. W. Horsell, and A. K. Savchenko, Phys. Rev. Lett. **98**, 176805 (2007).
[7] E. V. Castro, K. S. Novoselov, S. V. Morozov, N. M. R. Peres, J. M. B. Lopes dos Santos, J. Nilsson, F. Guinea, A. K. Geim, and A. H. Castro Neto, Phys. Rev. Lett. **99**, 216802 (2007).
[8] J. B. Oostinga, H. B. Heersche, X. Liu, A. F. Morpurgo, and L. M. K. Vandersypen, Nat. Mater. **7**, 151 (2008).
[9] P. R. Wallace, Phys. Rev. **71**, 622 (1947).
[10] J. C. Slonczewski and P. R. Weiss, Phys. Rev. **109**, 272 (1958).
[11] J. W. McClure, Phys. Rev. **108**, 612 (1957); **119**, 606 (1960).
[12] D. P. DiVincenzo and E. J. Mele, Phys. Rev. B **29**, 1685 (1984).
[13] G. W. Semenoff, Phys. Rev. Lett. **53**, 2449 (1984).
[14] T. Ando, T. Nakanishi, and R. Saito, J. Phys. Soc. Jpn. **67**, 2857 (1998).
[15] A. Bostwick, T. Ohta, T. Seyller, K. Horn, and E. Rotenberg, Nat. Phys. **3**, 36 (2007).
[16] S. Y. Zhou, G.-H. Gweon, J. Graf, A. V. Fedorov, C. D. Spataru, R. D. Diehl, Y. Kopelevich, D.-H. Lee, S. G. Louie, and A. Lanzara, Nat. Phys. **2**, 595 (2006).
[17] T. Ohta, A. Bostwick, J. L. McChesney, T. Seyller, K. Horn, and E. Rotenberg, Phys. Rev. Lett. **98**, 206802 (2007).
[18] A. Bostwick, T. Ohta, J. L. McChesney, K. V. Emtsev, T. Seyller, K. Horn, and E. Rotenberg, New J. Phys. **9**, 385 (2007).
[19] S. Y. Zhou, G.-H. Gweon, A. V. Fedorov, P. N. First, W. A. de Heer, D.-H. Lee, F. Guinea, A. H. Castro Neto, and A. Lanzara, Nat. Mater. **6**, 770 (2007).
[20] A. Bostwick, T. Ohta, J. L. McChesney, T. Seyller, K. Horn, and E. Rotenberg, Solid State Commun. **143**, 63 (2007).
[21] A. Bostwick, T. Ohta, J. L. McChesney, T. Seyller, K. Horn, and E. Rotenberg, Eur. Phys. J. Spec. Top. **148**, 5 (2007).
[22] C.-H. Park, F. Giustino, M. L. Cohen, and S. G. Louie, Phys. Rev. Lett. **99**, 086804 (2007).
[23] M. Calandra and F. Mauri, Phys. Rev. B **76**, 205411 (2007).
[24] W.-K. Tse and S. Das Sarma, Phys. Rev. Lett. **99**, 236802 (2007).
[25] M. Polini, R. Asgari, G. Borghi, Y. Barlas, T. Pereg-Barnea, and A. H. MacDonald, Phys. Rev. B **77**, 081411(R) (2008).
[26] E. McCann and V. I. Fal'ko, Phys. Rev. Lett. **96**, 086805 (2006).
[27] F. Guinea, A. H. Castro Neto, and N. M. R. Peres, Phys. Rev. B **73**, 245426 (2006).
[28] E. McCann, Phys. Rev. B **74**, 161403(R) (2006).
[29] H. Min, B. R. Sahu, S. K. Banerjee, and A. H. MacDonald, Phys. Rev. B **75**, 155115 (2007).
[30] M. Aoki and H. Amawashi, Solid State Commun. **142**, 123 (2007).
[31] E. McCann, D. S. L. Abergel, and V. I. Fal'ko, Solid State Com-

mun. **143**, 110 (2007).
[32] F. Guinea, A. H. Castro Neto, and N. M. R. Peres, Solid State Commun. **143**, 116 (2007).
[33] E. McCann, D. S. L. Abergel, and V. I. Fal'ko, Eur. Phys. J. Spec. Top. **148**, 91 (2007).
[34] F. Guinea, A. H. Castro Neto, and N. M. R. Peres, Eur. Phys. J. Spec. Top. **148**, 117 (2007).
[35] F. Varchon, R. Feng, J. Hass, X. Li, B. N. Nguyen, C. Naud, P. Mallet, J.-Y. Veuillen, C. Berger, E. H. Conrad, and L. Magaud, Phys. Rev. Lett. **99**, 126805 (2007).
[36] E. L. Shirley, L. J. Terminello, A. Santoni, and F. J. Himpsel, Phys. Rev. B **51**, 13614 (1995).
[37] F. J. Himpsel, Adv. Phys. **32**, 1 (1983).
[38] We define the charge-neutrality point as the position of the Fermi level in nominally undoped graphene and we set this position as that of zero energy. In monolayer graphene, this is often called the Dirac point.
[39] R. Saito, G. Dresselhaus, and M. S. Dresselhaus, *Physical Properties of Carbon Nanotubes* (Imperial College, London, 1998).
[40] M. S. Dresselhaus and G. Dresselhaus, Adv. Phys. **51**, 1 (2002).
[41] The tight-binding parameters are defined as $\gamma_0 = -\langle \Phi_{A1}|H|\Phi_{B1}\rangle = -\langle \Phi_{A2}|H|\Phi_{B2}\rangle$, where Φ_{A1} is an atomic orbital located on $A1$ site, $\gamma_1 = +\langle \Phi_{A2}|H|\Phi_{B1}\rangle$, $\gamma_3 = +\langle \Phi_{A1}|H|\Phi_{B2}\rangle$, and $\gamma_4 = +\langle \Phi_{A1}|H|\Phi_{A2}\rangle = +\langle \Phi_{B1}|H|\Phi_{B2}\rangle$. These definitions agree with those of the Slonczewski–Weiss–McClure model of graphite (Refs. 10 and 11). Note that the parameters describing interlayer hopping (γ_1, γ_3, and γ_4) enter the Hamiltonian of the Slonczewski–Weiss–McClure model with an additional factor of 2 that takes into account the greater number of neighboring graphene planes in bulk graphite as compared to bilayer graphene.
[42] In the absence of trigonal warping $\mu=0$, the intensity [Eq. (7)] in the presence of asymmetry Δ at low energy in monolayer graphene simplifies as $I \sim |\Phi_{\mathbf{p}}|^2\{1+[1-\Delta^2/(4\epsilon_q^2)]^{1/2}\cos(2\theta_1)\}\delta(E_{\mathbf{p}}+A-\epsilon_q-\hbar\omega)\delta_{\mathbf{q},\mathbf{p}_\parallel-\mathbf{K}_\pm-\mathbf{G}}$.
[43] B. Partoens and F. M. Peeters, Phys. Rev. B **74**, 075404 (2006).
[44] E. Mendez, A. Misu, and M. S. Dresselhaus, Phys. Rev. B **21**, 827 (1980).
[45] L. M. Malard, J. Nilsson, D. C. Elias, J. C. Brant, F. Plentz, E. S. Alves, A. H. Castro Neto, and M. A. Pimenta, Phys. Rev. B **76**, 201401(R) (2007).
[46] J.-C. Charlier, X. Gonze, and J.-P. Michenaud, Phys. Rev. B **43**, 4579 (1991).
[47] For emission from the conduction band at very low energy (top left side of Fig. 5), the interference pattern has two peaks [roughly similar to $\cos^2(\varphi)$], but one of the peaks has about three times stronger maximum intensity than the others. The reason is that corrections due to the presence of dimer orbitals are small (in parameter $\epsilon_q/\hbar v q$) but finite (this band has $\alpha=+1$). Their influence may be estimated by considering the function $g(\varphi) = 1+\cos(2\varphi)+4(\epsilon_q/\hbar v q)\cos(\varphi)+2(\epsilon_q/\hbar v q)^2$ [Eq. (10)]. Comparing the maxima of the two peaks, at angles $\varphi=0$ and $\varphi=\pi$, gives $g(0)/g(\pi)=[(1+\epsilon_q/\hbar v q)/(1-\epsilon_q/\hbar v q)]^2$. For the energy considered on the top left side of Fig. 5, where $\epsilon_q \approx \hbar^2 v^2 q^2/\gamma_1$, then $\epsilon_q/\hbar v q \approx (\epsilon_q/\gamma_1)^{1/2} \approx 0.29$. Thus, although this is "small," it yields $g(0)/g(\pi) \approx 3.34$.
[48] O. Betbeder-Matibet and M. Hulin, Phys. Status Solidi **36**, 573 (1969).
[49] P. Lawaetz, Solid State Commun. **16**, 65 (1975).
[50] ARPES spectra as described in Secs. III A and III B corresponding to photons with low energies, such that $p_z d \ll 1$ (d is the interlayer spacing), are the same for both twin crystals. To apply the results of Sec. III C to the $B2$-$A1$ twin, one would have to invert the signs of Δ and U. For higher photon energies, such that $\beta=p_z d$ is finite, the anisotropy maps in Fig. 9 of Sec. III D should be reflected with respect to the horizontal axis.